chemosensors

MDPI

Article

Fluorination vs. Chlorination: Effect on the Sensor Response of Tetrasubstituted Zinc Phthalocyanine Films to Ammonia

Dmitry Bonegardt [1], Darya Klyamer [1], Aleksandr Sukhikh [1], Pavel Krasnov [2], Pavel Popovetskiy [1] and Tamara Basova [1,*]

[1] Nikolaev Institute of Inorganic Chemistry SB RAS, 3 Lavrentiev Pr., 630090 Novosibirsk, Russia; bonegardt@niic.nsc.ru (D.B.); klyamer@niic.nsc.ru (D.K.); a_sukhikh@niic.nsc.ru (A.S.); popovetskiy@niic.nsc.ru (P.P.)

[2] International Research Center of Spectroscopy and Quantum Chemistry, Siberian Federal University, 660074 Krasnoyarsk, Russia; kpo1980@gmail.com

* Correspondence: basova@niic.nsc.ru; Tel.: +7-383-330-9556

Abstract: In this work, the effect of fluorine and chlorine substituents in tetrasubstituted zinc phthalocyanines, introduced into the non-peripheral ($ZnPcR_4$-np, R = F, Cl) and peripheral ($ZnPcR_4$-p, R = F, Cl) positions of macrocycle, on their structure and chemiresistive sensor response to low concentration of ammonia is studied. The structure and morphology of the zinc phthalocyanines films ($ZnPcR_4$) were investigated by X-ray diffraction and atomic force microscopy methods. To understand different effects of chlorine and fluorine substituents, the strength and nature of the bonding of ammonia and $ZnPcHal_4$ molecules were studied by quantum chemical simulation. It was shown on the basis of comparative analysis that the sensor response to ammonia was found to increase in the order $ZnPcCl_4$-np < $ZnPcF_4$-np < $ZnPcF_4$-p < $ZnPcCl_4$-p, which is in good agreement with the values of bonding energy between hydrogen atoms of NH_3 and halogen substituents in the phthalocyanine rings. $ZnPcCl_4$-p films demonstrate the maximal sensor response to ammonia with the calculated detection limit of 0.01 ppm; however, they are more sensitive to humidity than $ZnPcF_4$-p films. It was shown that both $ZnPcF_4$-p and $ZnPcCl_4$-p and can be used for the selective detection of NH_3 in the presence of carbon dioxide, dichloromethane, acetone, toluene, and ethanol.

Keywords: metal phthalocyanines; chemiresistive sensors; gas sensors; thin films; ammonia halogen substituents; crystal structure

Citation: Bonegardt, D.; Klyamer, D.; Sukhikh, A.; Krasnov, P.; Popovetskiy, P.; Basova, T. Fluorination vs. Chlorination: Effect on the Sensor Response of Tetrasubstituted Zinc Phthalocyanine Films to Ammonia. *Chemosensors* **2021**, *9*, 137. https://doi.org/10.3390/chemosensors9060137

Academic Editor: Vardan Galstyan

Received: 20 April 2021
Accepted: 9 June 2021
Published: 11 June 2021

1. Introduction

Ammonia is a highly irritating gas with a pungent smell. The problem of detecting ammonia is important in various sectors of agriculture and industry related to the production and use of fertilizers, as well as refrigeration systems [1]. In the last ten years, the diagnosis of various diseases by determining the concentration of biomarker gases in the exhaled air has attracted the attention of researchers and medical doctors [2–4]. It is known that ammonia is one of the biomarkers and its concentration > 1 ppm indicates renal failure in nephritis, atherosclerosis of the renal arteries, toxic affections of kidneys and other diseases [5]. There are a variety of sensing techniques existing for NH_3 detection, among them optical [6–8], electrochemical [9], surface acoustic [10,11], field effect transistor [12–14], and chemiresistive [15] sensors. Among them, chemiresistive gas sensors have attracted considerable attention in the field of sensor technology due to their advantages such as simplicity, low cost, and miniaturization capability [4,16]. Metal oxides, carbon nanomaterials, conductive polymer, and their hybrid materials are used as active layers of chemiresistive sensors for ammonia detection [17]. Metal phthalocyanines (MPc) also attract noticeable interest for sensing applications [18–20] due to their high sensitivity to different analytes, exceptional stability, versatile chemical system, and excellent processability resulting in the manufacture of thin films. Their properties can be tuned by introducing desirable

substituents into their aromatic rings. It was shown in previous works that introduction of electron withdrawing substituents (e.g., fluorine) led to an increase of MPc sensor response to reducing gases like ammonia and hydrogen [21,22]. Films of hexadecafluorosubstituted ($MPcF_{16}$) and tetrafluorosubstituted ($MPcF_4$-p) metal phthalocyanines with F-substituents in peripheral positions, deposited by vacuum evaporation, were studied as active layers of chemiresistive sensors for ammonia detection [22,23]. It was shown in our previous work [23] that the sensitivity of phthalocyanine films to ammonia increased in the order MPc < $MPcF_{16}$ < $MPcF_4$-p (M = Cu, Zn, Co). $MPcF_4$-p films were shown to be used as active layers for sensors to ammonia with the detection limit reaching 0.1 ppm. Apart from this, they allow ammonia to be detected in the presence of carbon dioxide, some volatile organic compounds and at high humidity. These properties make fluorosubstituted metal phthalocyanines very promising for the detection of low concentration of ammonia in the gas mixtures.

In the case of tetrafluorosubstituted phthalocyanines, the F-substituents can be introduced not only to peripheral positions (Figure 1), but also to non-peripheral ones. The literature analysis has shown that studies of $MPcF_4$-np thin films were only sporadic [24,25], and their sensor properties have not yet been studied. Chlorination is also a common method used to modify the behavior of the π-conjugated molecular semiconductors [26]. Although Cl (electronegativity is 3.16) is less electronegative than F (electronegativity is 3.98), its empty 3d orbit can help to accept π electrons in the system, resulting in the stronger ability of chlorination to decrease than fluorination to downshift the molecular energy levels in comparison with fluorination. Chlorosubstituted metal phthalocyanines ones are also widely investigated. Similarly to MPcFx, films of chlorosubstituted $MPcCl_x$ can also be deposited by thermal evaporation [27–31]. Parameters of crystal cell of $CuPcCl_x$ (x = 4, 8, 16) have been determined by Fryer and co-authors [32] using the method of electron diffraction, while later the single crystal structure of $CuPcF_4$-np have been refined [33]. $CuPcCl_x$ was shown to demonstrate semiconductor properties with the lower HOMO and LUMO energy levels compared to unsubstituted CuPc [34,35]. The charge carrier mobility of $CuPcCl_{16}$ films was shown to be about 10^{-2} cm^2 V^{-1} s^{-1} [36]. Achar et al. [37] found that the conductivity of $CuPcCl_4$ pellets was four orders of magnitude higher than that in the case of unsubstituted CuPc. At the same time, the chemiresistive properties of chlorosubstituted metal phthalocyanines have not yet been investigated.

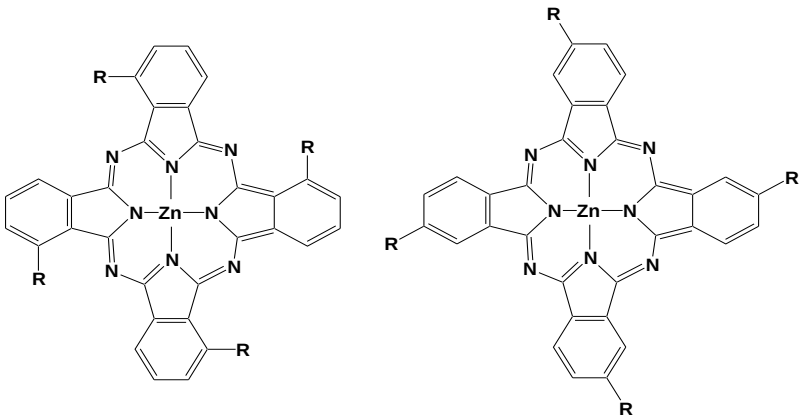

$ZnPcR_4$-np **$ZnPcR_4$-p**

Figure 1. Structure of tetrahalogensubstituted zinc phthalocyanines bearing F or Cl-substituents in non-peripheral ($ZnPcF_4$-np) and peripheral ($ZnPcF_4$-p) positions (R = F or Cl).

These latest results raise the question of how to choose between fluorinated and chlorinated phthalocyanines when designing materials for chemiresistive sensors with good sensor characteristics.

In this work, the effect of the position of fluorine and chlorine substituents in tetrasubstituted zinc phthalocyanines $ZnPcR_4$-np and $ZnPcF_4$-p (R = F, Cl) (Figure 1) on their

structure and chemiresistive sensor response to low concentration of ammonia is studied. The structure and morphology of the films of tetrafluoro- and tetrachlorosubstituted zinc phthalocyanines, deposited by thermal evaporation vacuum, were investigated by X-ray diffraction (XRD) and atomic force microscopy (AFM) methods. On the basis of comparative analysis, the films with the best sensor characteristics (sensitivity, selectivity, detection limits, response and recovery times) were chosen.

2. Materials and Methods

Zinc phthalocyanine derivatives were synthesized according to the techniques described elsewhere [22] from zinc acetate and corresponding phthalonitrile derivatives. 4-fluorophthalonitrile (Aldrich), 3-fluorophthalonitrile (FluoroChem), 4-chlorophthalonitrile, and 3-chlorophthalonitrile (Abcr) were used for the synthesis of $ZnPcF_4$-p, $ZnPcF_4$-np, $ZnPcCl_4$-p, and $ZnPcCl_4$-np, respectively. 4-chlorophthalonitrile was synthesized from 4-aminophthalonitrile (Acros Organics, Geel, Belgium) according to the procedure described by Antunes and Nyokong [38]. Both $ZnPcF_4$ and $ZnPcCl_4$ derivatives contained a statistical mixture of regioisomers due to the various possible positions of fluorine and chlorine substituents, which were not separated because of close parameters of sublimation. The synthesized phthalocyanines were purified by double sublimation in vacuum (10^{-5} Torr) at 450–460 °C.

Thin films were deposited by an organic molecular beam deposition technique on glass substrates or glass slides with predeposited Pt interdigitated electrodes. The substrate temperature was about 60 °C. The nominal thickness of the films was about 100 nm.

Crystal structures were determined at 150 K using a Bruker D8 Venture single-crystal diffractometer (Incoatec IμS 3.0 MoKα microfocus tube, PHOTON III C14 charge-integrating pixel array detector, fixed-chi 3-circle goniometer, Cryostream 800 Plus open-flow nitrogen cooler). APEX3 V2018.7-2 software package (SAINT 8.38A, SADABS-2016/2) [39] was used for the raw data collection, data reduction, absorption correction and global unit cell refinement. Obtained hkl datasets were processed in Olex2 v.1.2.10 [40] using SHELXT 2018/2 [41] and SHELXL 2018/3 [42] for the structure solution and refinement, respectively. Thin film XRD patterns were recorded on a Shimadzu XRD-7000 powder diffractometer (Bragg-Brentano scheme with vertical θ-θ goniometer, CuKα sealed tube with Ni foil β-filter, OneSight silicon strip detector).

Atomic force microscopy (AFM) in semi-contact mode with a Ntegra Prima II (NT-MDT, Russia) microscope was used for the characterization of films morphology. The HA_NC (A) tip had the following parameters: length—123 μm, width—34 μm, thickness—3 μm, force constant—17 N/m, resonance frequency—230 kHz. The roughness parameters were calculated using the Nova SPM software according to the standards ISO 4287-1, ISO 4287 and ASME B46.

For testing the chemiresistive sensor response the films were deposited onto the platinum interdigitated electrodes (Dropsens, Spain). The electrodes had the following dimensions: gap between digits—10 μm; number of digits—125 × 2 with a digit length of 6760 μm; cell constant—0.0118 cm^{-1}. The interdigitated electrodes with a deposited phthalocyanine film were placed in a homemade gas flow cell and kept for 15 min under the air flow until their resistance reached a steady value. The scheme of the system for investigation of the chemiresistive sensor response with a photo of the gas flow cell is shown in Figure 2. The required gas flow was regulated using mass flow regulators. The electrical resistance of ZnPc films, which changed when interacting with the analyte gas, was measured using a Keithley 236 electrometer by applying a constant DC voltage (10 V).

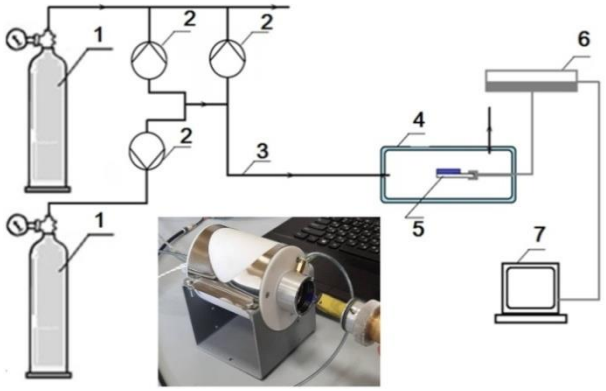

Figure 2. Scheme of the system for investigation of chemiresistive sensor response with a photograph of a gas flow cell: 1—tanks with a gaseous analyte and purging/diluent gas, 2—mass flow controllers, 3—gas mixture with a given analyte concentration, 4—gas flow cell, 5—active layer, 6—electrometer, 7—computer.

Then, the analyte gas of the required concentration and the air used for purging were alternately introduced into the cell. The sensor response of the films was determined after alternation of exposure and recovery periods in a dynamic regime in most experiments. The injection of NH_3 was carried out at the constant air flow rate of 300 mL/min and the exposure time was fixed at 30 s. The determination of the response and recovery times of the sensing layer was performed in a static regime. In this case, the air stream flowed through the test chamber until the resistance reached a state value, and then the valves of the chamber were closed and diluted NH_3 gas was injected into the cell. The resistance was recorded during a period of time necessary to obtain saturation value and calculate the response time of the sensor. Afterwards, the chamber was opened and was purged with air flow. For humidity measurements, the wet carrier gas was prepared by bubbling the carrier gas through distilled water. The relative humidity (RH) inside the cell was controlled with a commercially available humidity meter (MPE-202.013).

Theoretical Calculations

The nature of bonding between zinc phthalocyanines and ammonia was studied by performing a topological analysis of the electron density distribution function in these molecules in the framework of the Quantum Theory "Atoms in Molecules" (QTAIM) [43,44]. These functions were obtained as a result of quantum-chemical calculations carried out in the ORCA software package [45,46], using the DFT B3LYP/def2-SVP method [47–51], semiempirical dispersion potential Grimme [52,53], RI approximation [54–59], and auxiliary basis set Def2/J [60]. In the search of the equilibrium geometric structure of the molecules, no symmetry restrictions were used (the point group of symmetry C_1). The spin multiplet was equal to one, which corresponded to energetically more favorable electronic states.

The absence of negative frequencies in the vibrational spectra of the molecules in addition to their minimum total energies was the criterion for achieving an equilibrium geometric structure. The binding energy (E_b) of $ZnPcHal_4$ with the NH_3 molecule was calculated from the difference in the total energies of the corresponding structure and its components:

$$E_b = E_{NH_3} + E_{ZnPcHal_4} - E_{ZnPcHal_4\cdots NH_3} - \Delta E_{BSSE}, \quad (1)$$

where ΔE_{BSSE} is the correction to the binding energy, taking into account the basis set superposition error (BSSE), which was estimated as follows:

$$\Delta E_{BSSE} = \left(E^{ZnPcHal_4\cdots NH_3}_{ZnPcHal_4} + E^{ZnPcHal_4\cdots NH_3}_{NH_3}\right) - \left(E^{ZnPcHal_4\cdots NH_3}_{ZnPcHal_4*} + E^{ZnPcHal_4\cdots NH_3}_{NH_3*}\right). \quad (2)$$

The upper index in Equation (2) indicates that the geometries of $ZnPcHal_4$ and NH_3 were taken from the optimized $ZnPcHal_4 \cdots NH_3$ structure, while the geometric structures of ZnPcHal and NH_3 were not optimized, but only their electronic structures were calculated. The asterisks in the lower indices mean which fragment of the $ZnPcHal_4 \cdots NH_3$ aggregate is considered, whereas the atoms of the other fragment are considered as the points described by the corresponding atomic basis sets.

Additionally, the binding energies were calculated for comparison by another more accurate method, where the structure geometries and zero-point energies were taken from the DFT results, while electronic energies were estimated in the framework of the DLPNO-CCSD(T)/def2-TZVPP approach [50,60–63] without taking into account the BSSE correction. This approach represents the domain-based local pair natural orbital (DLPNO) approximation implemented to speed up the coupled-cluster method with single and double excitations and perturbative triple excitations (CCSD(T)), employs localized occupied orbitals, and allows us to get the correlation energy as the sum of the correlation energies of the electron pairs [62–64].

In the QTAIM approach, an indicator of the binding interaction of two atoms is the presence of the bond critical point (3, −1) (BCP) between them. Herein $\omega = 3$ is a Hessian matrix rank at this point, and $\sigma = -1$ is a sum of signs of Hessian matrix eigenvalues λ_i ($\lambda_1 < 0$, $\lambda_2 < 0$ и $\lambda_3 > 0$). The set of values of these parameters, including the Laplacian of the electron density $\nabla^2\rho(r) = \lambda_1 + \lambda_2 + \lambda_3$, can be used to estimate the nature of the atoms' interaction under consideration. In particular, if $|\lambda_1|/\lambda_3 > 1$ ($\nabla^2\rho(r) < 1$), the so-called shared interaction occurs. The electron density is accumulated and distributed in the interatomic space, which is typical for covalent bonds. In the case where $|\lambda_1|/\lambda_3 < 1$ ($\nabla^2\rho(r) > 1$), the closed-shell interaction is observed, which is characteristic of ionic, strongly polar covalent, hydrogen and van der Waals bonds [43,44,65,66]. In this case, there is an outflow of electron density from the critical point to the atomic nuclei. There is also an intermediate interaction, in which the value of $\nabla^2\rho(r)$ is also positive, but the chemical bond is considered covalent if the value of $\rho(r)$ is large. In this case, one resorts to the analysis of additional quantities, such as, for example, the electron energy density h(r). A negative value of this value at the corresponding critical point of the bond is considered a sufficient condition for the bond to be considered covalent [44].

3. Results and Discussion

3.1. Crystal Structure of $ZnPcCl_4$-p and $ZnPcCl_4$-np

Crystal structure of $ZnPcF_4$-p has been investigated by our group earlier [67]. $ZnPcF_4$-p crystallizes in P-1 space group with Z = 1 and is isomorphous to α-polymorphs of unsubstituted phthalocyanines, such as α-CuPc [68] and α-CoPc [69]. $ZnPcF_4$-p molecules are arranged in stacks (Figure 3a) with a distance of 3.331 Å between the molecules inside the stack (the distance between the planes drawn through all non-hydrogen atoms) and a stacking angle of 25.31° (the angle between the stacking direction and the normal to the plane). The structure of $ZnPcF_4$-np crystals grown by vacuum sublimation in this work was identical to that described by Hui Jiang et al. [70]. $ZnPcF_4$-np crystallizes in the $P2_1/n$ space group with Z = 2 and is isomorphous to the β-polymorph of ZnPc [71]. $ZnPcF_4$-np molecules are arranged in a herringbone pattern (Figure 3b) with a distance of 3.258 Å between the molecules within the stack, a stacking angle of 47.29° and an angle between molecules in adjacent stacks of 85.42°. $ZnPcCl_4$-p crystallizes in the $I4_1/a$ space group with Z = 8 (Z′ = 0.5). $ZnPcCl_4$-p molecules are also packed in stacks with a distance of 3.392 Å between the molecules within the stack and a stacking angle 20.81°, while the angle between the molecules in adjacent stacks is 29.12° and the adjacent stacks are rotated 90° relative to each other (Figure 3c).

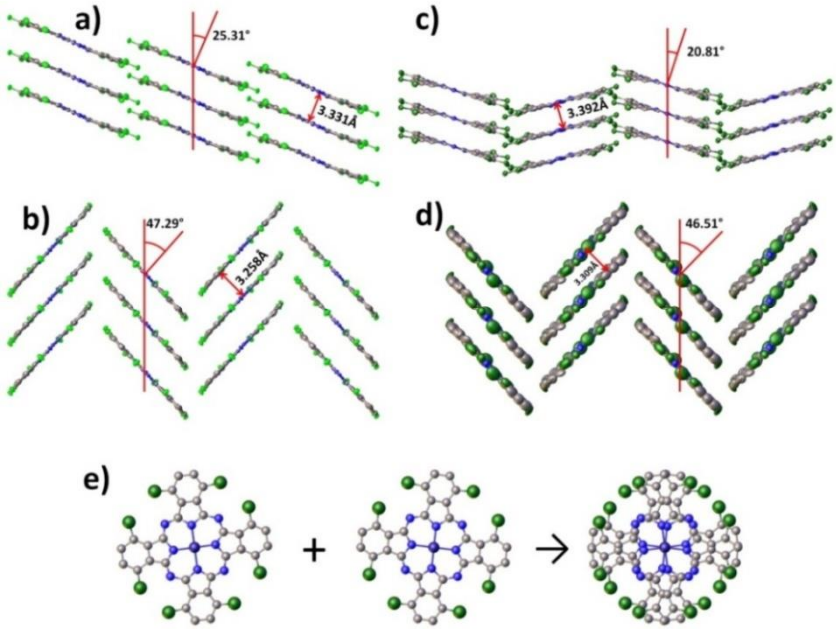

Figure 3. Molecule packing diagrams for $ZnPcF_4$-p (**a**), $ZnPcF_4$-np (**b**), $ZnPcCl_4$-p (**c**), ZnPcCl4-np (**d**); disorder of ZnPcCl4-np molecules (**e**).

$ZnPcCl_4$-np crystallizes in the $P2_1/n$ space group. A distance between the molecules in the stack is 3.309 Å, a stacking angle is 46.51° and an angle between molecules in adjacent stacks is 86.97° (Figure 3d). At first glance, $ZnPcCl_4$-np is isomorphic to both $ZnPcF_4$-np and β-ZnPc, but the substituents of the chlorine atoms are too bulky compared to fluorine and hydrogen, which leads to very close contacts between the molecules in adjacent stacks. As a result, one $ZnPcCl_4$-np molecule is rotated relative to the other in the plane around the central Zn atom by about 13° (Figure 3e). This leads to the fact that all the atoms, except for Zn and Cl, are disordered in two positions with a ratio of 0.56:0.44. Since each Cl atom can already occupy two equivalent positions in the molecule, they are disordered over four positions each, with the ratios of 0.19:0.45:0.29:0.07 and 0.13:0.36:0.44:0.07 ratios. F and Cl atoms are also disordered over two positions each in other tetrahalogenated ZnPc derivatives with the following ratios: 0.56:0.44 and 0.52:0.48 for $ZnPcF_4$-p, 0.61:0.39 and 0.54:0.46 for $ZnPcF_4$-np, 0.52:0.48 and 0.54:0.46 for $ZnPcCl_4$-p.

It should also be noted that the molecules of all four investigated $ZnPcHal_4$ derivatives remain relatively flat; the maximum deviation of any non-hydrogen atom from the root-mean-square plane is 0.168 Å for $ZnPcF_4$-p, 0.103 Å for $ZnPcF_4$-np, 0.232 Å for $ZnPcCl_4$-p and 0.216 Å for $ZnPcCl_4$-np (cf. 0.116 Å for ZnPc). The unit cell parameters and refinement statistics for $ZnPcF_4$-np, $ZnPcCl_4$-p and $ZnPcCl_4$-np are given in Table 1.

Table 1. Unit cell parameters and refinement details.

Compound	$ZnPcF_4$-np	$ZnPcCl_4$-p	$ZnPcCl_4$-np
Empirical formula	$C_{32}H_{12}F_4N_8Zn$	$C_{32}H_{12}Cl_4N_8Zn$	$C_{32}H_{12}Cl_4N_8Zn$
Formula weight	649.87	715.67	715.67
Temperature/K	150.0	150.0	150.0
Crystal system	monoclinic	tetragonal	monoclinic
Space group	$P2_1/n$	$I4_1/a$	$P2_1/n$
a/Å	14.8240(17)	38.3949(13)	14.4126(15)
b/Å	4.8033(7)	38.3949(13)	4.8075(5)
c/Å	17.866(2)	3.6284(2)	20.331(2)

Table 1. *Cont.*

Compound	$ZnPcF_4$-np	$ZnPcCl_4$-p	$ZnPcCl_4$-np
α/°	90	90	90
β/°	108.039(7)	90	110.544(3)
γ/°	90	90	90
Volume/Å^3	1209.6(3)	5348.9(5)	1319.1(2)
Z	2	8	2
ρ_{calc}g/cm^3	1.784	1.777	1.792
F(000)	652	2864	716
Independent reflections	2293 [Rint = 0.0818, Rsigma = 0.0751]	4075 [Rint = 0.0575, Rsigma = 0.0371]	1895 [Rint = 0.0684, Rsigma = 0.0519]
Data/restraints/ parameters	2293/0/226	4075/0/226	1895/310/400
Goodness-of-fit on F2	1.014	1.120	1.042
Final R indexes [I >= 2σ (I)]	R1 = 0.0479, wR2 = 0.0800	R1 = 0.0460, wR2 = 0.0871	R1 = 0.0581, wR2 = 0.1547
Final R indexes [all data]	R1 = 0.0833, wR2 = 0.0910	R1 = 0.0553, wR2 = 0.0900	R1 = 0.1015, wR2 = 0.1806
CCDC deposition №	2077055	2077056	2077057

3.2. Structure and Morphology of Thin Films

Thin film XRD patterns of $ZnPcHal_4$ in the range of 4–30° 2θ are shown in Figure 4 in comparison with the powder patterns calculated using the above-mentioned data on the single-crystal structure and unit cell parameters.

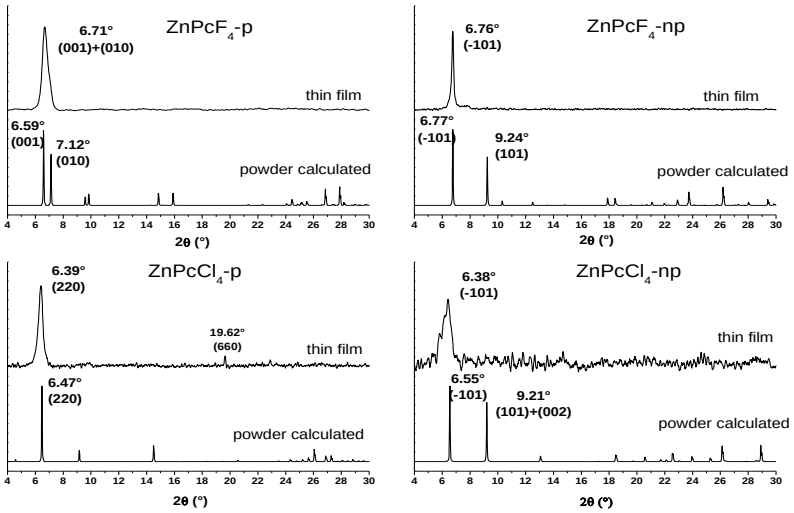

Figure 4. X-ray diffraction patterns of $ZnPcHal_4$ thin film in comparison with the calculated powder XRD patterns.

XRD patterns of all $ZnPcHal_4$ films have single diffraction peaks, which indicate a possible strong preferred orientation of the film. The diffraction peak on the XRD pattern of $ZnPcF_4$-p film has a noticeable asymmetry on the right side, and the 2θ position of its maximum at 6.71° lies between the peak (001) at 6.59° and the peak (010) at 7.12°, which means that the preferred orientation in the film is not ideal, and although most crystallites are oriented by the plane (001) parallel to the substrate surface, some are oriented by the plane (010) parallel to the surface substrates. The 2θ position of the diffraction peak on

the XRD pattern of $ZnPcF_4$-np film coincides well with the peak (−101) on the calculated powder pattern. The $ZnPcF_4$-np film has a stronger preferred orientation and better crystallinity compared to the $ZnPcF_4$-p film, since the diffraction peak on its X-ray image has a significantly lower FWHM (0.15°) compared to that of $ZnPcF_4$-p (0.5°).

The XRD pattern of $ZnPcCl_4$-p film has a strong diffraction peak at 6.39° 2θ with FWHM of 0.37°, which corresponds to (220) peak at 6.47° 2θ on the calculated powder pattern. A small peak at 19.62° 2θ corresponds to the peak (660), which belongs to the same group of crystallographic planes as the peak (220). The XRD pattern of $ZnPcCl_4$-np film has a single weak broad peak at 6.38° 2θ with FWHM of 0.83°, which corresponds to the peak (−101) at 6.55° 2θ on the calculated powder pattern. Its low intensity and high FWHM value suggest that the $ZnPcCl_4$-np film has very poor crystallinity compared to the films of other investigated phthalocyanines. The angles between the molecules and the substrate surface in $ZnPcHal_4$ films, calculated on the basis of XRD data, are shown in Figure 5.

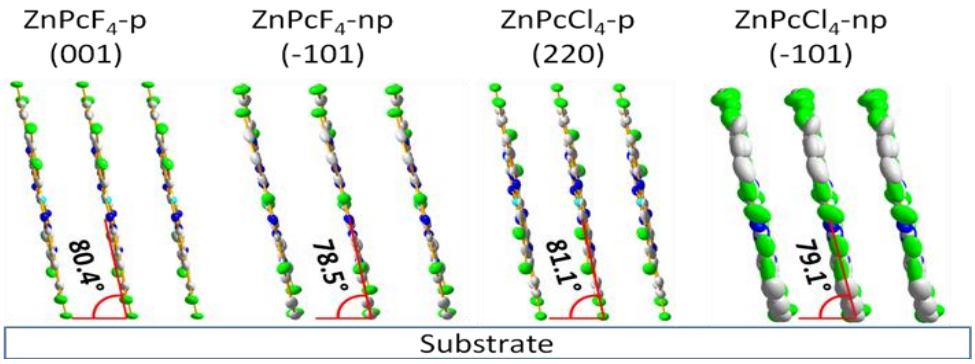

Figure 5. Orientation of $ZnPcHal_4$ molecules relative to the substrate surface in the films.

The morphology of the films was studied by AFM (Figure 6). The morphology of $ZnPcF_4$-np and $ZnPcF_4$-p films is very similar. The surface of both films consists of slightly elongated crystallites with the size reaching 0.07 μm. The RMS values of $ZnPcF_4$-np and $ZnPcF_4$-np film are 9.54 and 4.44 nm, respectively. The film of $ZnPcCl_4$-p consists of the clearly distinguishable smaller crystallites and has RMS of 5.58 nm. The morphology of the $ZnPcCl_4$-p film differs significantly from that of the films of $ZnPcCl_4$-p; the film is formed by vague elongated agglomerates, the size of which reaches 0.4 μm. Its RMS value is 8.96 nm.

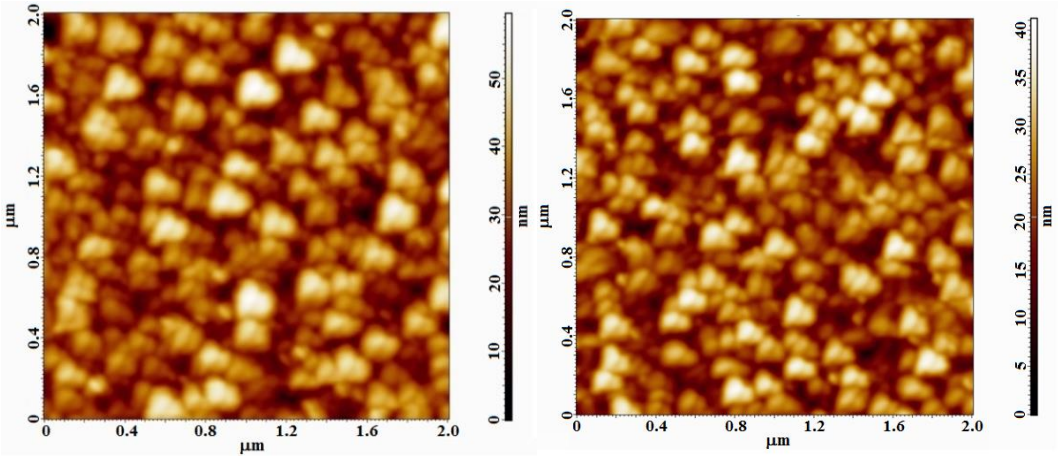

(**a**) (**b**)

Figure 6. *Cont.*

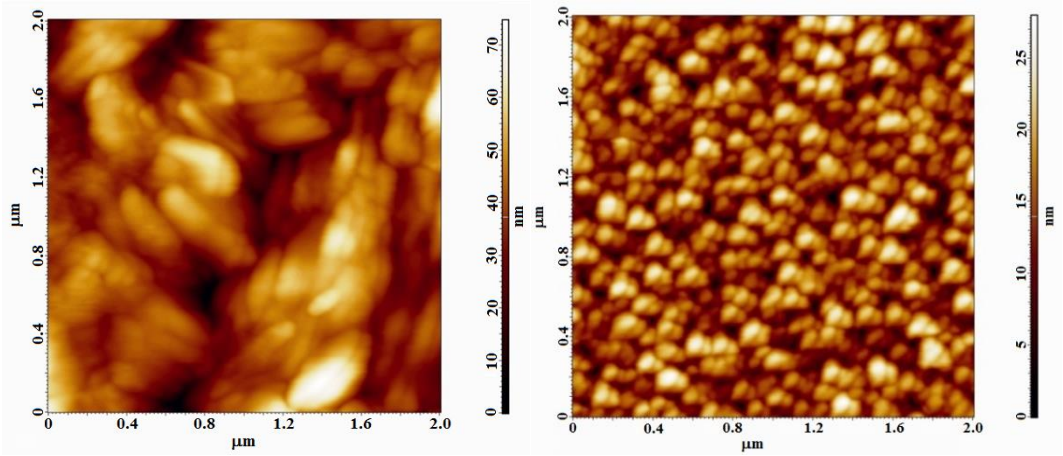

Figure 6. Atomic force microscopy images of $ZnPcF_4$-np (**a**), $ZnPcF_4$-p (**b**), $ZnPcCl_4$-np (**c**), and $ZnPcCl_4$-p (**d**) films.

3.3. Sensor Response of $ZnPcHal_4$ Films to Ammonia

The effect of the type of halogen substituents and their positions in the phthalocyanine ring on the sensor response toward gaseous ammonia (0.1–50 ppm) was studied in order to choose the material with the best sensor performance. The typical response S of the sensor, defined as $S = (R - R_o)/R_o$, where R is the resistance of a phthalocyanine film at a certain concentration of NH_3 and R_o is the initial resistance of the film in fresh air, is shown in Figure 7a as an example.

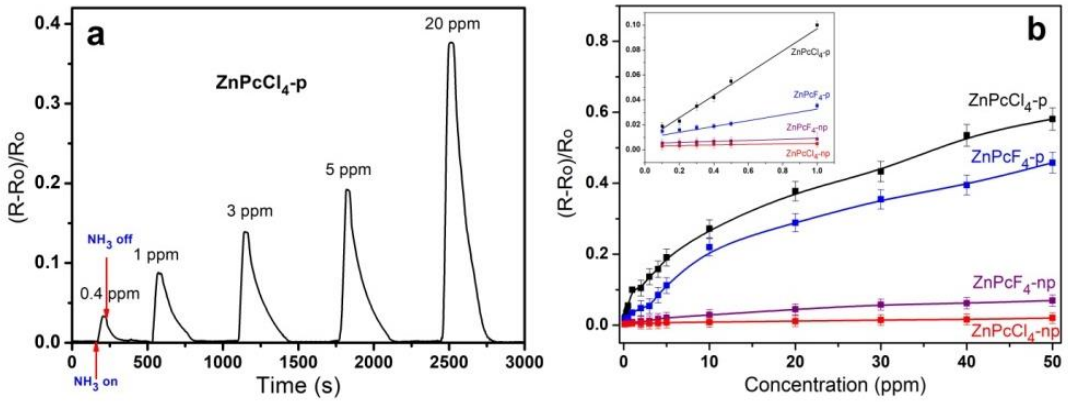

Figure 7. (**a**) Real-time sensor response of a $ZnPcCl_4$-p film to ammonia, measured at RH 10% and 25 °C. (**b**) Dependence of the sensor response of $ZnPcF_4$-np, $ZnPcF_4$-p, $ZnPcCl_4$-np, and $ZnPcCl_4$-p sensing layers on ammonia concentration.

All sensing layers showed a noticeable increase in the resistance when exposed to ammonia. When the ammonia supply was stopped, the resistance was restored to its initial value, which indicated fast response and reversibility of the investigated sensors toward ammonia at room temperature. This behavior is typical for p-type organic semiconductors, and has also been observed for other unsubstituted and tetrafluorinated metal phthalocyanines [23]. Based on the fact that the studied phthalocyanines are p-type semiconductors, it was expected that their exposure to NH_3 would cause an increase in the resistance due to depletion of the positively charged holes by electrons donated by NH_3 molecules [72,73].

The dependence of the sensor response of investigated sensing layers on ammonia concentration is presented in Figure 7b. The sensor response of the investigated layers was found to increase in the order $ZnPcCl_4$-np < $ZnPcF_4$-np < $ZnPcF_4$-p < $ZnPcCl_4$-p. For example, the sensor response of $ZnPcCl_4$-p film to 1 ppm NH_3 is 2 times higher than that of the $ZnPcF_4$-np film and 17 times higher than that of the $ZnPcCl_4$-np film.

The linear dependence of the sensor response on the ammonia concentration is observed in the range from 0.1 to 1 ppm, and at higher concentrations the curve deviates from the linear one. The detection limits (LOD) of the sensing layers were estimated as *3s/m*, where *m* is the slope of the calibration plot in the linear region, while *s* is the standard deviation of the sensor response to 1 ppm of NH_3 (Figure 7b inset).

LODs were calculated to be 0.01 ppm for the films of $ZnPcCl_4$-p and $ZnPcF_4$-p, while its values were 0.08 and 0.1 ppm in the case of $ZnPcF_4$-np and $ZnPcCl_4$-np films, respectively. The response and recovery time of phthalocyanine layers toward ammonia (1 ppm) was also investigated as presented in Figure 8 and summarized in Table 2.

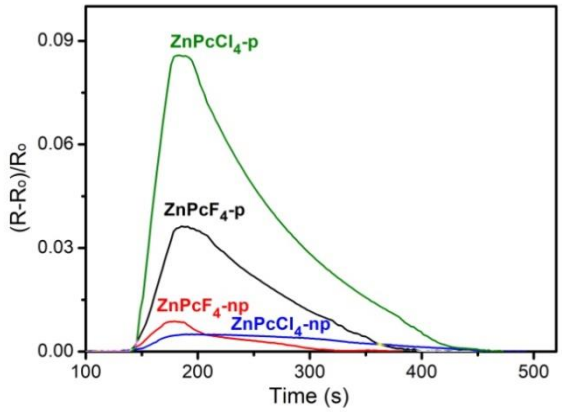

Figure 8. Response-recovery time of the $ZnPcHal_4$ sensing layers at 1 ppm ammonia, measured at room temperature and RH 10%.

Table 2. Calculated detection limits and response/recovery times (at 1ppm NH_3) of $ZnPcF_4$-np, $ZnPcF_4$-p, $ZnPcCl_4$-np, and $ZnPcCl_4$-p sensing layers.

Sensing Layer	Calculated LOD, ppm	Response Time, s	Recovery Time, s
$ZnPcF_4$-np	0.08	35	155
$ZnPcF_4$-p	0.01	45	210
$ZnPcCl_4$-np	0.1	45	280
$ZnPcCl_4$-p	0.01	45	260

3.4. Theoretical Study of the Nature of Bonding between Ammonia and $ZnPcHal_4$ Molecules

Although observations of changes in the measured current of MPc sensing layers exposed to NH_3 and other analytes are explained by electron transfer, the interaction sites in the phthalocyanine macrocycle or metal center are still a matter of discussion. According to the data of most works, the most energetically favorable cite of NH_3 molecule binding is the central metal of MPc molecules [23,74,75]. In the case of the non-planar lead phthalocyanines, two bond critical points characterized the considered interaction between NH_3 and $PbPcF_x$ were observed: between the Pb and nitrogen atoms as well as between one of the hydrogen atoms of ammonia and the N_β atom of the $PbPcF_x$ macrocycle [76]. These conclusions were based only on quantum chemical calculations. At the same time, the experimental investigations of the interaction sites are sporadic [77]. Chia et al. [77] used in situ X-ray absorption spectroscopy (XAS) for the investigation of interaction of CuPc with NH_3 molecule. The first derivative of XANES suggested low or lack of axial position coordination on the Cu metal center. On the other hand, the interaction on the macrocycle was supported by the EXAFS. From the EXAFS of CuPc with NH_3, the interaction was suggested to be at the benzene ring or bridging nitrogen atom. The experimental investigations of the interaction sites in the case of halogen-substituted MPcs have not yet been carried out.

In this work, the strength and nature of the bonding of ammonia and $ZnPcHal_4$ molecules were studied using quantum chemical simulation to understand the different

effects of chlorine and fluorine substituents. It is known than there are two possible positions for the binding of NH_3 molecule in $ZnPcHal_4$, namely central metal and substituents. For this reason, we considered the interaction between NH_3 and $ZnPcHal_4$ both via the central metal and through peripheral and non-peripheral halogen atoms.

The binding energy between the central metal (Zn) and nitrogen of ammonia in $ZnPcHal_4 \cdots NH_3$ aggregates seemed to be very similar and only slightly increased in the order $ZnPcF_4$-p (−18.4 kcal/mol) < $ZnPcF_4$-np (−18.4 kcal/mol) < $ZnPcCl_4$-np (−18.6 kcal/mol) < $ZnPcCl_4$-p (−18.6 kcal/mol). The energy values were close, but a different trend was obtained with the use of the more accurate DLPNO-CCSD(T)/def2-TZVPP method: $ZnPcF_4$-np (−18.5 kcal/mol) < $ZnPcCl_4$-np (−18.8 kcal/mol) < $ZnPcF_4$-p (−21.2 kcal/mol) < $ZnPcCl_4$-p (−21.3 kcal/mol). The binding energy was approximately 3 kcal/mol higher in the case of phthalocyanines bearing halogen substituents in peripheral positions.

It is important to note that the interaction of an isolated phthalocyanine molecule with NH_3 is considered in quantum-chemical calculations. In fact, in polycrystalline films, the molecules are packed in stacks of parallel molecules with a distance between the aromatic rings of about 3.3–3.4 Å (Figure 3), which is not enough for the penetration of NH_3 molecules between them to the central metal. Therefore, such interaction seems unlikely or possible only with the terminal molecules in the stacks. This, apparently, explains the results obtained in the work of Chia et al. [77] cited above. In addition, the estimated energies (20–24 kcal/mol) look high enough to be responsible for the sensor response to ammonia, which is easily reversible at room temperature.

Thus, it was also reasonable to consider the interactions of ammonia with $ZnPcHal_4$ molecules via peripheral and non-peripheral halogen atoms. For this purpose, the topological analysis of the electron density distribution function was carried out. As a result, the corresponding bond critical points were established (Figure 9), and the values of $\rho(\mathbf{r})$ and $\nabla^2\rho(\mathbf{r})$ at these points were estimated. It was shown that the $ZnPcCl_4$-np$\cdots NH_3$ aggregate is characterized by the presence of three bond critical points: two between the hydrogen atoms of the ammonia molecule and the chlorine atom of $ZnPcCl_4$-np (BCP1 and BCP2, Figure 9) and one between the nitrogen atom of NH_3 and the non-peripheral hydrogen atom of $ZnPcCl_4$-np (BCP3). Similarly, three BCPs characterizing the interaction of NH_3 molecule with phthalocyanines are observed for $ZnPcCl_4$-p$\cdots NH_3$, but, in contrast to the previous case, BCP2 is located between the nitrogen atom of NH_3 and the non-peripheral hydrogen atom of the benzene ring, which contains the chlorine atom involved in the formation of BCP1.

Phthalocyanines with fluorine substituents are characterized by two bond critical points (BCP1 and BCP2). BCP1 is observed between one of the hydrogen atoms of ammonia and the F atom, and BCP2 is between the nitrogen atom of NH_3 and the non-peripheral hydrogen atom. The difference between $ZnPcF_4$-np$\cdots NH_3$ and $ZnPcF_4$-p$\cdots NH_3$ is that in the case of BCP2, the hydrogen atoms are located on different benzene rings. The parameters of almost all designated BCPs indicate the formation of hydrogen bonds between these pairs of atoms. This follows from the fact that the $\rho(\mathbf{r})$ и $\nabla^2\rho(\mathbf{r})$ values in almost all cases lie in the ranges of 0.013–0.236 e/Å^3 and 0.578–3.350 e/Å^5, respectively, which are characteristic of a hydrogen bond (Table 3) [44,78]. Only for BCP3 in $ZnPcCl_4$-p$\cdots NH_3$, the values of the electron density and its Laplacian are significantly lower than the lower limit of these ranges, thus the interaction of the corresponding pair of atoms is rather of the Van der Waals type [79].

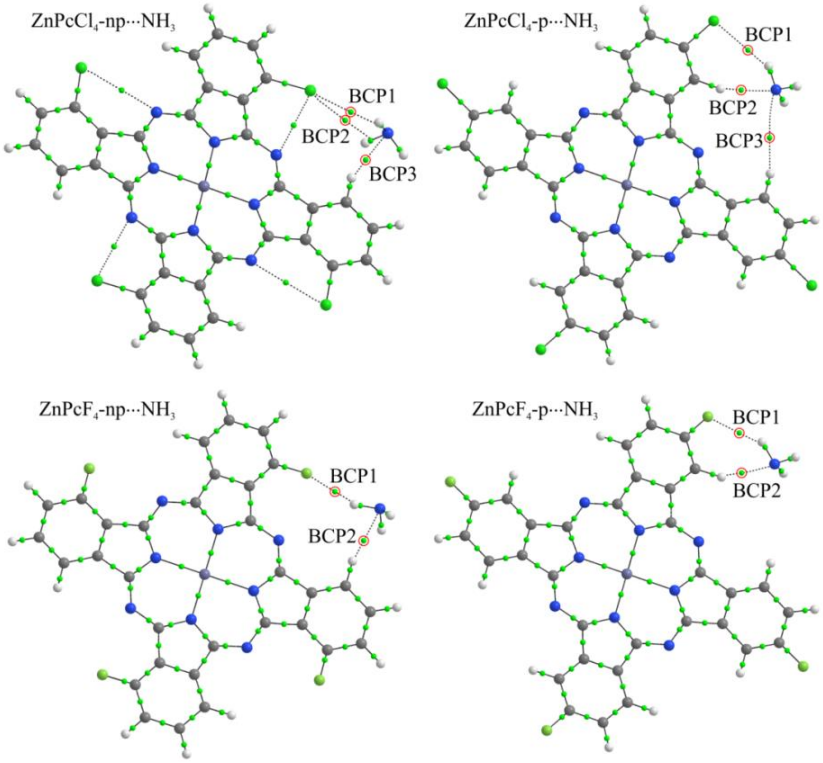

Figure 9. Geometric structure of $ZnPcHal_4 \cdots NH_3$ aggregates. Small green balls show the positions of the bond critical points (3, −1) (the points indicating the formation of a bond between phthalocyanine and ammonia are highlighted in red).

Table 3. Topological parameters of the $\rho(\mathbf{r})$ function in the bond critical points between atoms of ammonia and $ZnPcHal_4$ molecules.

Structure	BCP	$\rho(\mathbf{r})$, e/Å^3	$\nabla^2\rho(\mathbf{r})$, e/Å^5	$\lvert\lambda_1\rvert/\lambda_3$	$h_e(\mathbf{r})$, a.u.	E_b, kcal/mol
$ZnPcCl_4$-np···NH_3	1	0.045	0.674	0.137	$1.21 \cdot 10^{-3}$	−0.9 (−0.1 *)
	2	0.045	0.672	0.138	$1.18 \cdot 10^{-3}$	
	3	0.069	0.628	0.180	$3.50 \cdot 10^{-4}$	
$ZnPcCl_4$-p···NH_3	1	0.059	0.579	0.199	$2.16 \cdot 10^{-4}$	−3.5 (−3.7 *)
	2	0.113	0.972	0.238	$-6.60 \cdot 10^{-5}$	
	3	0.006	0.075	0.140	$2.74 \cdot 10^{-4}$	
$ZnPcF_4$-np···NH_3	1	0.077	1.003	0.194	$2.38 \cdot 10^{-4}$	−1.5 (−1.0 *)
	2	0.075	0.665	0.187	$2.34 \cdot 10^{-4}$	
$ZnPcF_4$-p···NH_3	1	0.065	0.845	0.196	$3.99 \cdot 10^{-4}$	−3.2 (−3.1 *)
	2	0.110	0.967	0.235	$-4.00 \cdot 10^{-6}$	

* E_b values calculated using the DLPNO-CCSD(T)/def2-TZVPP method.

As a rule, hydrogen bonds are characterized by the *closed-shell interaction* between two atoms [44,78,79]. This interaction is characterized by small values of $\rho(\mathbf{r})$ and $\nabla^2\rho(\mathbf{r})$ at the corresponding critical point (3, −1), while the values of $\nabla^2\rho(r)$ are positive [43,44,65,66]. Besides, the ratio of eigenvalues ($\lvert\lambda_1\rvert/\lambda_3$) of the electron density Hessian matrix at this point in the case of *closed-shell interaction* is less than one, which is also observed for all considered BCPs (Table 3). However, negative values of the local electron energy $h_e(\mathbf{r})$ in BCP2 in the case of $ZnPcCl_4$-p···NH_3 and $ZnPcF_4$-p···NH_3 indicate the *intermediate interaction* between the corresponding pairs of atoms, which could be an indicator of covalent bonds formation [79]. At the same time, the values of $\rho(\mathbf{r})$ at these points are low enough to suggest the formation of covalent bonds; however, they are significantly higher than the electron density values at all other critical points of the bond considered here. It is this fact that determines a stronger binding of the NH_3 molecule with ZnPc derivatives

bearing Cl and F substituents in peripheral positions. Finally, the absolute value of E_b increases in the order $ZnPcCl_4$-np$\cdots NH_3$ < $ZnPcF_4$-np$\cdots NH_3$ < $ZnPcF_4$-p$\cdots NH_3$ < $ZnPcCl_4$-p$\cdots NH_3$ (Table 3), which is in good agreement with the experimental data. Moreover, calculated Gibbs free energy change values at 298 K are close to zero in all four cases, indicating the reversibility of the NH_3 molecule binding with phthalocyanines. The same tendency of E_b change was obtained by additional calculations with the use of the DLPNO-CCSD(T)/def2-TZVPP method (Table 3, the values of E_b in parentheses).

In this type of interaction, the binding of NH3 molecules can occur simultaneously with several phthalocyanine molecules, which leads to an increase in the total energy of the interaction. At the same time, the energy remains sufficiently low, which ensures the reversibility of sorption-desorption of analyte molecules.

3.5. Sensor Characteristics of $ZnPcCl_4$-p and $ZnPcF_4$-p Films

Sensor characteristics of $ZnPcCl_4$-p and $ZnPcF_4$-p films showing the best sensitivity to ammonia were studied in more detail to demonstrate the possibility of their use for the determination of low concentrations of ammonia in air. The reproducibility of the response of ZnPcR4 layers was studied by repeated exposure to 0.4 ppm NH_3 over a certain period of time, as shown in Figure 10a. Both sensors showed reproducible response after gas-on and gas-off cycle measurements for about one hour. The long-term stability of the sensing layers was also tested by an experiment with 0.4 ppm NH_3 at room temperature. The inset of Figure 10a shows that no more than 6% decrease of the sensor response of a $ZnPcCl_4$-p film to ammonia was observed after 120 days, which testify its good stability. To investigate the effects of the relative humidity (RH), the response of both $ZnPcF_4$-p and $ZnPcCl_4$-p films was tested at different RH values. Figure 10b shows the change of the films' resistance upon exposure to 30–50 ppm NH_3 at 10, 40, and 70% RH. It was shown that an increase in humidity up to 40% did not lead to a change in the initial resistance of the $ZnPcF_4$-p film and its sensor response to ammonia, but with an increase in humidity up to 70%, a decrease in the sensor response by about 1.5 times was observed (Figure 10c). This decrease in the sensor response can be explained by competitive sorption of the NH_3 and H_2O molecules on the surface of a $ZnPcF_4$-p film. This behavior is consistent with previously reported results [23,80]. At the same time, the films of $ZnPcCl_4$-p are more sensitive to humidity. An increase of the humidity led to the more pronounced decrease in the initial resistance of $ZnPcCl_4$-p film than in the case of $ZnPcF_4$-p (Figure 10b). In contrast to $ZnPcF_4$-p films, the sensor response of a $ZnPcCl_4$-p film to ammonia increased with a growth of humidity up to 70% (Figure 10d).

The binding energies of H_2O with $ZnPcCl_4$-p and $ZnPcF_4$-p molecules, calculated using the same method as with ammonia, were shown to be −3.0 and −2.7 kcal/mol, respectively. A stronger interaction between H_2O and $ZnPcCl_4$-p may promote the adsorption of more water molecules on the film surface. In the conditions of high humidity a continuous water layer appears to form on the surface of $ZnPcCl_4$-p film and physisorbed water layers become to show a liquidlike behavior. Similar behavior was also described by authors of previous work [81,82], and the mechanism describing the increase in the conductivity of sensitive layers at high RH of the environment is known as the Grottuss mechanism [81]. Protons (H^+) formed as a result of water dissociation can move more easily through the water layer, which leads to an increase in the conductivity of the sensing film. With the introduction of NH_3, the formation of NH^{4+} and OH^- ions generated from the dissociation of NH_3 in water may facilitate an increase in the sensor response, similar to the case described by other researchers [82,83].

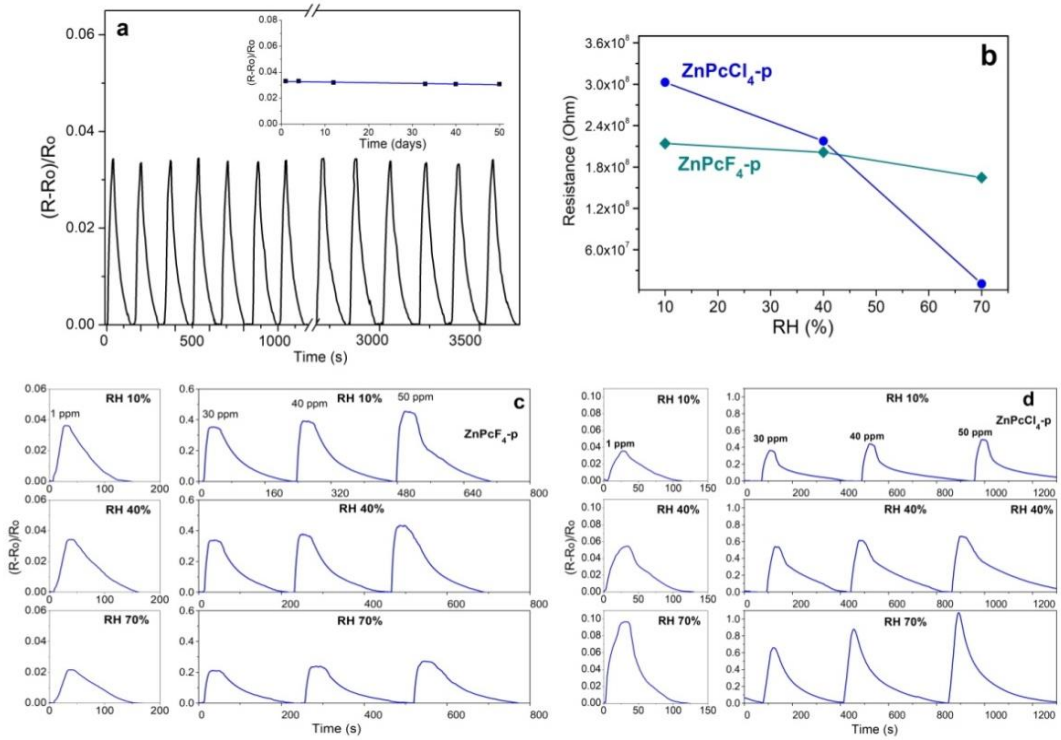

Figure 10. (**a**) Reproducibility and stability of the response of a $ZnPcCl_4$-p layer to 0.4 ppm NH_3, measured at room temperature and RH 10%. Change of the resistance (**b**) and the sensor response (**c**,**d**) of the $ZnPcF_4$-p and $ZnPcCl_4$-p films upon interaction with NH_3 at different relative humidity, measured at room temperature.

Selectivity is another important factor for the application of chemical sensors. To investigate the selectivity, the response of the layers of $ZnPcF_4$-p and $ZnPcCl_4$-p to various analytes, viz. carbon dioxide, dichloromethane, acetone, toluene, ethanol, was tested (Figure 11). It is obvious that the response of both sensing layers to NH_3 was much higher than to interfering analytes. It is necessary to mention that the concentration of ammonia given in the diagram is much less than that of the other analytes. These results show that the sensors are highly selective against the tested interfering analytes, especially at their low concentrations, which makes them attractive for detecting ammonia in gas mixtures.

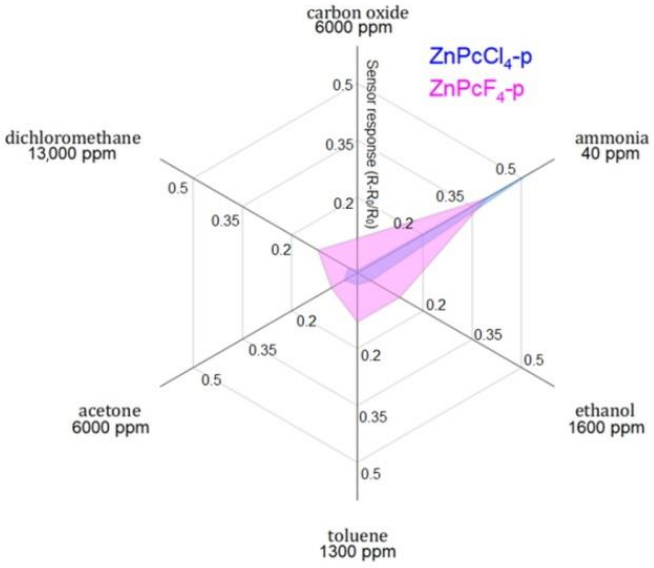

Figure 11. Diagram of selectivity of $ZnPcF_4$-p and $ZnPcCl_4$-p sensing layers toward various analytes, measured at room temperature and RH 10%.

The sensor response of a $ZnPcCl_4$-p film to ammonia was also measured in the mixture of air with carbon dioxide (10,000 ppm) (Figure 12). It was found that the presence of 10,000 ppm CO_2 has virtually no effect on the sensitivity of the $ZnPcCl_4$-p film to ammonia, e.g., the $(R - R_o)/R_o$ value increased from 0.38 to 0.44 when 10,000 ppm CO_2 was added to the gas mixture containing 20 ppm NH_3. It was also shown (Figure 12) that the heating of the films to 100 °C did not cause noticeable changes of the sensitivity of $ZnPcCl_4$-p film to ammonia.

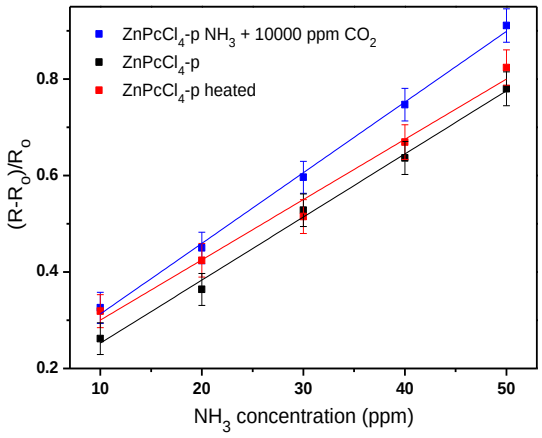

Figure 12. Sensor response of a $ZnPcCl_4$-p film to ammonia (10–50 ppm) and to ammonia in the presence of 10,000 ppm CO_2, measured at RH 10% and 25 °C and after heating to 100 °C.

Some examples of chemiresistive sensors on the basis of phthalocyanine films described in the literature are presented in Table 4 and compared with the results obtained in this work. Both $ZnPcF_4$-p and $ZnPcCl_4$-p films exhibit the lower detection limit in comparison with the films of other metal phthalocyanines.

Table 4. Sensor characteristics of various phthalocyanines toward ammonia.

Sensing Layer	Method	Concentration Range, ppm	Minimal Investigated Concentration, ppm	Response/ Recovery Time, s	Temp. Range, °C	Refs.
CuPc	chemiresistive	0.5–2	0.5	60/120 (0.5 ppm)	RT	[77]
CoPc	chemiresistive	20–100	20	~60/240 (23 ppm)	RT	[84]
$CoPcR_8$, R is 5-(trifluorome-thyl)-2-mer-captopyridine	chemiresistive	0.3–50	0.3	20/40 (5 ppm)	RT	[80]
PdPc	chemiresistive	10–50	10	25/50 (10 ppm)	RT	[21]
FCrPc	chemiresistive	40–100	40	10/13 (40 ppm)	100–400	[85]
$ZnPcF_{16}$	SPR *	100–200	100	10/30 (100 ppm)	RT	[86]
$ZnPcF_4$-p	chemiresistive	0.1–50	0.1	45/210	RT	this work
$ZnPcCl_4$-p	chemiresistive	0.1–50	0.1	45/260 (1 ppm)	RT	this work

* Surface plasmon resonance.

4. Conclusions

In this work, the effect of the position of fluorine and chlorine substituents in tetra-substituted zinc phthalocyanines $ZnPcR_4$-np and $ZnPcF_4$-p (R = F, Cl) on their structure and chemiresistive sensor response to low concentration of ammonia was studied. The structure and morphology of their films deposited by thermal evaporation in vacuum were investigated by XRD and atomic force microscopy methods. It was shown that both position and type of substituents affect the structure of single crystals and films of zinc phthalocyanines. In the case of $ZnPcF_4$-p, the molecules are arranged in parallel stacks

similarly to α-polymorphs of unsubstituted phthalocyanines, while $ZnPcF_4$-np, $ZnPcCl_4$-p and $ZnPcCl_4$-np form crystals and films with herring bone arrangements of phthalocyanine macrocycles. According to XRD data, the films of have strong preferential orientation of crystallites relative to the substrate surface; however, the $ZnPcCl_4$-np film has poorer crystallinity compared to the films of other phthalocyanine derivatives.

The chemiresistive sensor response of the investigated layers to ammonia was found to increase in the order $ZnPcCl_4$-np < $ZnPcF_4$-np < $ZnPcF_4$-p < $ZnPcCl_4$-p, which is in good agreement with the values of bonding energy between hydrogen atoms of NH_3 and halogen substituents in the phthalocyanine rings. $ZnPcCl_4$-p films demonstrate the maximal sensor response to ammonia with the calculated detection limit of 0.01 ppm. Additionally, the sensors have good long-term stability and reproducibility. It was shown that both $ZnPcF_4$-p and $ZnPcCl_4$-p and can be used for the selective detection of ammonia in the presence of carbon dioxide, dichloromethane, acetone, toluene, and ethanol.

Author Contributions: Conceptualization, T.B. and A.S.; methodology, D.K. and A.S.; validation, D.K., A.S. and D.B.; investigation, D.K., A.S., D.B. and P.P.; writing (original draft preparation), D.K., T.B. and A.S.; writing (review and editing), T.B. and P.K.; visualization, A.S. and P.K.; supervision, A.S. and T.B.; project administration, A.S.; funding acquisition, A.S. All authors have read and agreed to the published version of the manuscript.

Funding: Russian Science Foundation (project number 20-73-00080).

Institutional Review Board Statement: Not applicable.

Informed Consent Statement: Not applicable.

Data Availability Statement: Not applicable.

Acknowledgments: D.B. and A.S. acknowledge Russian Science Foundation (project number 20-73-00080) for the financial support.

Conflicts of Interest: The authors declare no conflict of interest.

References

1. Timmer, B.; Olthuis, W.; Van Den Berg, A. Ammonia sensors and their applications—A review. *Sens. Actuators B Chem.* **2005**, *107*, 666–677. [CrossRef]
2. Saasa, V.; Malwela, T.; Beukes, M.; Mokgotho, M.; Liu, C.-P.; Mwakikunga, B. Sensing Technologies for Detection of Acetone in Human Breath for Diabetes Diagnosis and Monitoring. *Diagnostics* **2018**, *8*, 12. [CrossRef] [PubMed]
3. Marzorati, D.; Mainardi, L.; Sedda, G.; Gasparri, R.; Spaggiari, L.; Cerveri, P. A Review of Exhaled Breath Key Role in Lung Cancer Diagnosis. *J. Breath Res.* **2017**, *13*, 034001. [CrossRef]
4. Yoon, J.W.; Lee, J.H. Toward breath analysis on a chip for disease diagnosis using semiconductor-based chemiresistors: Recent progress and future perspectives. *Lab Chip* **2017**, *17*, 3537–3557. [CrossRef] [PubMed]
5. Righettoni, M.; Amann, A.; Pratsinis, S.E. Breath analysis by nanostructured metal oxides as chemo-resistive gas sensors. *Mater. Today* **2015**, *18*, 163–171. [CrossRef]
6. Hodgkinson, J.; Tatam, R.P. Optical gas sensing: A review. *Meas. Sci. Technol.* **2013**, *24*, 012004. [CrossRef]
7. Claps, R.; Englich, F.V.; Leleux, D.P.; Richter, D.; Tittel, F.K.; Curl, R.F. Ammonia detection by use of near-infrared diode-laser-based overtone spectroscopy. *Appl. Opt.* **2001**, *40*, 4387. [CrossRef] [PubMed]
8. Miller, D.J.; Sun, K.; Tao, L.; Khan, M.A.; Zondlo, M.A. Open-path, quantum cascade-laser-based sensor for high-resolution atmospheric ammonia measurements. *Atmos. Meas. Tech.* **2014**, *7*, 81–93. [CrossRef]
9. Sekhar, P.K.; Kysar, J.S. An Electrochemical Ammonia Sensor on Paper Substrate. *J. Electrochem. Soc.* **2017**, *164*, B113–B117. [CrossRef]
10. Shen, C.Y.; Huang, C.P.; Huang, W.T. Gas-detecting properties of surface acoustic wave ammonia sensors. *Sens. Actuators B Chem.* **2004**, *101*, 1–7. [CrossRef]
11. Chen, X.; Li, D.M.; Liang, S.F.; Zhan, S.; Liu, M. Gas sensing properties of surface acoustic wave NH3 gas sensor based on Pt doped polypyrrole sensitive film. *Sens. Actuators B Chem.* **2013**, *177*, 364–369. [CrossRef]
12. Han, S.; Zhuang, X.; Jiang, Y.; Yang, X.; Li, L.; Yu, J. Poly(vinyl alcohol) as a gas accumulation layer for an organic field-effect transistor ammonia sensor. *Sens. Actuators B Chem.* **2017**, *243*, 1248–1254. [CrossRef]
13. Han, S.; Zhuang, X.; Shi, W.; Yang, X.; Li, L.; Yu, J. Poly(3-hexylthiophene)/polystyrene (P3HT/PS) blends based organic field-effect transistor ammonia gas sensor. *Sens. Actuators B Chem.* **2016**, *225*, 10–15. [CrossRef]
14. Besar, K.; Yang, S.; Guo, X.; Huang, W.; Rule, A.M.; Breysse, P.N.; Kymissis, I.J.; Katz, H.E. Printable ammonia sensor based on organic field effect transistor. *Org. Electron.* **2014**, *15*, 3221–3230. [CrossRef]

15. Zhao, Y.M.; Zhu, Y.Q. Room temperature ammonia sensing properties of W18O49 nanowires. *Sens. Actuators B Chem.* **2009**, *137*, 27–31. [CrossRef]
16. Kwak, D.; Lei, Y.; Maric, R. Ammonia gas sensors: A comprehensive review. *Talanta* **2019**, *204*, 713–730. [CrossRef] [PubMed]
17. Aarya, S.; Kumar, Y.; Chahota, R.K. Recent Advances in Materials, Parameters, Performance and Technology in Ammonia Sensors: A Review. *J. Inorg. Organomet. Polym. Mater.* **2020**, *30*, 269–290. [CrossRef]
18. Rydosz, A.; Maciak, E.; Wincza, K.; Gruszczynski, S. Microwave-based sensors with phthalocyanine films for acetone, ethanol and methanol detection. *Sens. Actuators B Chem.* **2016**, *237*, 876–886. [CrossRef]
19. Chani, M.T.S.; Karimov, K.S.; Ahmad Khalid, F.; Raza, K.; Umer Farooq, M.; Zafar, Q. Humidity sensors based on aluminum phthalocyanine chloride thin films. *Phys. E Low-Dimens. Syst. Nanostruct.* **2012**, *45*, 77–81. [CrossRef]
20. Zhihua, L.; Xucheng, Z.; Jiyong, S.; Xiaobo, Z.; Xiaowei, H.; Tahir, H.E.; Holmes, M. Fast response ammonia sensor based on porous thin film of polyaniline/sulfonated nickel phthalocyanine composites. *Sens. Actuators B Chem.* **2016**, *226*, 553–562. [CrossRef]
21. Parkhomenko, R.G.; Sukhikh, A.S.; Klyamer, D.D.; Krasnov, P.O.; Gromilov, S.; Kadem, B.; Hassan, A.K.; Basova, T.V. Thin Films of Unsubstituted and Fluorinated Palladium Phthalocyanines: Structure and Sensor Response toward Ammonia and Hydrogen. *J. Phys. Chem. C* **2017**, *121*, 1200–1209. [CrossRef]
22. Klyamer, D.D.; Sukhikh, A.S.; Krasnov, P.O.; Gromilov, S.A.; Morozova, N.B.; Basova, T.V. Thin films of tetrafluorosubstituted cobalt phthalocyanine: Structure and sensor properties. *Appl. Surf. Sci.* **2016**, *372*, 79–86. [CrossRef]
23. Klyamer, D.; Sukhikh, A.; Gromilov, S.; Krasnov, P.; Basova, T. Fluorinated metal phthalocyanines: Interplay between fluorination degree, films orientation, and ammonia sensing properties. *Sensors* **2018**, *18*, 2141. [CrossRef] [PubMed]
24. Mayer, T.; Weiler, U.; Kelting, C.; Schlettwein, D.; Makarov, S.; Wöhrle, D.; Abdallah, O.; Kunst, M.; Jaegermann, W. Silicon–organic pigment material hybrids for photovoltaic application. *Sol. Energy Mater. Sol. Cells* **2007**, *91*, 1873–1886. [CrossRef]
25. Oksengendler, I.G.; Kondratenko, N.V.; Luk'yanets, E.A.; Yagupol'skii, L.M. Fluoro-and perfluoro-tert-butyl-substituted phthalocyanines. *Zh. Org. Khim* **1977**, *13*, 2234.
26. Tang, M.L.; Bao, Z. Halogenated Materials as Organic Semiconductors. *Chem. Mater.* **2010**, *23*, 446–455. [CrossRef]
27. Pakhomov, L.G.; Pakhomov, G.L. NO_2 interaction with thin film of phthalocyanine derivatives {1}. *Synth. Met.* **1995**, *71*, 2299–2300. [CrossRef]
28. Irie, S.; Hoshino, A.; Kuwamoto, K.; Isoda, S.; Miles, M.J.; Kobayashi, T. Point-on-line coincidence in epitaxial growth of CuPcCl 16 on graphite. *Appl. Surf. Sci.* **1997**, *113–114*, 310–315. [CrossRef]
29. Mittelberger, A.; Kramberger, C.; Meyer, J.C. Insights into radiation damage from atomic resolution scanning transmission electron microscopy imaging of mono-layer $CuPcCl_{16}$ films on graphene. *Sci. Rep.* **2018**, *8*, 4813. [CrossRef]
30. Yoshida, K.; Biskupek, J.; Kurata, H.; Kaiser, U. Critical conditions for atomic resolution imaging of molecular crystals by aberration-corrected HRTEM. *Ultramicroscopy* **2015**, *159*, 73–80. [CrossRef]
31. Bobaru, S.C.; Salomon, E.; Layet, J.-M.; Angot, T. Structural Properties of Iron Phtalocyanines on Ag(111): From the Submonolayer to Monolayer Range. *J. Phys. Chem. C* **2011**, *115*, 5875–5879. [CrossRef]
32. Fryer, J.R. Electron Crystallography of Phthalocyanines. *J. Porphyr. Phthalocyanines* **1999**, *3*, 672–678. [CrossRef]
33. Sukhikh, A.; Bonegardt, D.; Klyamer, D.; Krasnov, P.; Basova, T. Chlorosubstituted copper phthalocyanines: Spectral study and structure of thin films. *Molecules* **2020**, *25*, 1620. [CrossRef] [PubMed]
34. Selvaraj, T.; Rajalingam, R. Theoretical Studies of the Zeolite-Y Encapsulated Chlorine-Substituted Copper(II)phthalocyanine Complex on the Formation Glycidol from Allyl Alcohol. *ACS Omega* **2018**, *3*, 9613–9619. [CrossRef]
35. Sahoo, S.R.; Sahu, S.; Sharma, S. Charge transport and prototypical optical absorptions in functionalized zinc phthalocyanine compounds: A density functional study. *J. Phys. Org. Chem.* **2018**, *31*, e3785. [CrossRef]
36. Ling, M.-M.; Bao, Z.; Erk, P. Air-stable n-channel copper hexachlorophthalocyanine for field-effect transistors. *Appl. Phys. Lett.* **2006**, *89*, 163516. [CrossRef]
37. Achar, B.N.; Jayasree, P.K. "Molecular Metals" Based on Copper(II) 2,9,16,23-tetrahalo Substituted Phthalocyanine Derivatives. *Synth. React. Inorg. Met. Chem.* **2000**, *30*, 719–733. [CrossRef]
38. Antunes, E.M.; Nyokong, T. Synthesis and Photophysical Properties of Tetra- and Octasubstituted Phosphorous Oxide Triazatetrabenzcorrole Photosensitizers. *Met. Based. Drugs* **2008**, *2008*, 498916. [CrossRef]
39. Bruker AXS Inc. *Bruker Advanced X-ray Solutions*; Bruker: Madison, WI, USA, 2004.
40. Dolomanov, O.V.; Bourhis, L.J.; Gildea, R.J.; Howard, J.A.K.; Puschmann, H. OLEX2: A complete structure solution, refinement and analysis program. *J. Appl. Crystallogr.* **2009**, *42*, 339–341. [CrossRef]
41. Sheldrick, G.M. SHELXT-Integrated space-group and crystal-structure determination. *Acta Crystallogr. Sect. A Found. Crystallogr.* **2015**, *71*, 3–8. [CrossRef]
42. Sheldrick, G.M. Crystal structure refinement with SHELXL. *Acta Crystallogr. Sect. C Struct. Chem.* **2015**, *71*, 3–8. [CrossRef] [PubMed]
43. Bader, R.F.W.; Essén, H. The characterization of atomic interactions. *J. Chem. Phys.* **1984**, *80*, 1943–1960. [CrossRef]
44. Bushmarinov, I.S.; Lyssenko, K.A.; Antipin, M.Y. Atomic energy in the "Atoms in Molecules" theory and its use for solving chemical problems. *Russ. Chem. Rev.* **2009**, *78*, 283–302. [CrossRef]
45. Neese, F. The ORCA program system. *Wiley Interdiscip. Rev. Comput. Mol. Sci.* **2012**, *2*, 73–78. [CrossRef]

46. Neese, F. Software update: The ORCA program system, version 4.0. *Wiley Interdiscip. Rev. Comput. Mol. Sci.* **2018**, *8*, e1327. [CrossRef]
47. Hohenberg, P.; Kohn, W. Inhomogeneous Electron Gas. *Phys. Rev. B* **1964**, *136*, B864–B871. [CrossRef]
48. Becke, A.D. Density-functional thermochemistry. III. The role of exact exchange. *J. Chem. Phys.* **1993**, *98*, 5648–5652. [CrossRef]
49. Vosko, S.H.; Wilk, L.; Nusair, M. Accurate spin-dependent electron liquid correlation energies for local spin density calculations: A critical analysis. *Can. J. Phys.* **1980**, *58*, 1200–1211. [CrossRef]
50. Weigend, F.; Ahlrichs, R. Balanced basis sets of split valence, triple zeta valence and quadruple zeta valence quality for H to Rn: Design and assessment of accuracy. *Phys. Chem. Chem. Phys.* **2005**, *7*, 3297–3305. [CrossRef]
51. Lee, C.; Yang, W.; Parr, R.G. Development of the Colle-Salvetti correlation-energy formula into a functional of the electron density. *Phys. Rev. B* **1988**, *37*, 785–789. [CrossRef]
52. Grimme, S.; Antony, J.; Ehrlich, S.; Krieg, H. A consistent and accurate ab initio parametrization of density functional dispersion correction (DFT-D) for the 94 elements H-Pu. *J. Chem. Phys.* **2010**, *132*, 154104. [CrossRef] [PubMed]
53. Grimme, S.; Ehrlich, S.; Goerigk, L. Effect of the damping function in dispersion corrected density functional theory. *J. Comput. Chem.* **2011**, *32*, 1456–1465. [CrossRef] [PubMed]
54. Baerends, E.J.; Ellis, D.E.; Ros, P. Self-consistent molecular Hartree-Fock-Slater calculations I. The computational procedure. *Chem. Phys.* **1973**, *2*, 41–51. [CrossRef]
55. Dunlap, B.I.; Connolly, J.W.D.; Sabin, J.R. On some approximations in applications of Xα theory. *J. Chem. Phys.* **1979**, *71*, 3396–3402. [CrossRef]
56. Van Alsenoy, C. Ab initio calculations on large molecules: The multiplicative integral approximation. *J. Comput. Chem.* **1988**, *9*, 620–626. [CrossRef]
57. Kendall, R.A.; Früchtl, H.A. The impact of the resolution of the identity approximate integral method on modern ab initio algorithm development. *Theor. Chem. Acc.* **1997**, *97*, 158–163. [CrossRef]
58. Eichkorn, K.; Weigend, F.; Treutler, O.; Ahlrichs, R. Auxiliary basis sets for main row atoms and transition metals and their use to approximate Coulomb potentials. *Theor. Chem. Acc.* **1997**, *97*, 119–124. [CrossRef]
59. Eichkorn, K.; Treutler, O.; Öhm, H.; Häser, M.; Ahlrichs, R. Auxiliary basis sets to approximate Coulomb potentials (Chem. Phys. Letters 240 (1995) 283) (PII:0009-2614(95)00621-4). *Chem. Phys. Lett.* **1995**, *242*, 652–660. [CrossRef]
60. Weigend, F. Accurate Coulomb-fitting basis sets for H to Rn. *Phys. Chem. Chem. Phys.* **2006**, *8*, 1057–1065. [CrossRef]
61. Riplinger, C.; Sandhoefer, B.; Hansen, A.; Neese, F. Natural triple excitations in local coupled cluster calculations with pair natural orbitals. *J. Chem. Phys.* **2013**, *139*, 134101. [CrossRef]
62. Riplinger, C.; Neese, F. An efficient and near linear scaling pair natural orbital based local coupled cluster method. *J. Chem. Phys.* **2013**, *138*, 034106. [CrossRef]
63. Pinski, P.; Riplinger, C.; Valeev, E.F.; Neese, F. Sparse maps—A systematic infrastructure for reduced-scaling electronic structure methods. I. An efficient and simple linear scaling local MP2 method that uses an intermediate basis of pair natural orbitals. *J. Chem. Phys.* **2015**, *143*, 034108. [CrossRef]
64. Sandler, I.; Chen, J.; Taylor, M.; Sharma, S.; Ho, J. Accuracy of DLPNO-CCSD(T): Effect of Basis Set and System Size. *J. Phys. Chem. A* **2021**, *125*, 1553–1563. [CrossRef]
65. Bader, R.F.W. A quantum theory of molecular structure and its applications. *Chem. Rev.* **1991**, *91*, 893–928. [CrossRef]
66. Bader, R.F.W. *Atom in Molecules: A Quantum Theory*; Oxford University Press: New York, NY, USA, 1994.
67. Klyamer, D.D.; Sukhikh, A.S.; Gromilov, S.A.; Kruchinin, V.N.; Spesivtsev, E.V.; Hassan, A.K.; Basova, T.V. Influence of fluorosubstitution on the structure of zinc phthalocyanine thin films. *Macroheterocycles* **2018**, *11*, 304–311. [CrossRef]
68. Hoshino, A.; Takenaka, Y.; Miyaji, H. Redetermination of the crystal structure of α-copper phthalocyanine grown on KCl. *Acta Crystallogr. Sect. B Struct. Sci.* **2003**, *59*, 393–403. [CrossRef] [PubMed]
69. Ballirano, P.; Caminiti, R.; Ercolani, C.; Maras, A.; Orrù, M.A. X-ray powder diffraction structure reinvestigation of the α and β forms of cobalt phthalocyanine and kinetics of the α → β phase transition. *J. Am. Chem. Soc.* **1998**, *120*, 12798–12807. [CrossRef]
70. Jiang, H.; Hu, P.; Ye, J.; Li, Y.; Li, H.; Zhang, X.; Li, R.; Dong, H.; Hu, W.; Kloc, C. Molecular Crystal Engineering: Tuning Organic Semiconductor from p-type to n-type by Adjusting Their Substitutional Symmetry. *Adv. Mater.* **2017**, *29*, 1605053. [CrossRef]
71. Scheidt, W.R.; Dow, W. Molecular Stereochemistry of Phthalocyanatozinc(II). *J. Am. Chem. Soc.* **1977**, *99*, 1101–1104. [CrossRef]
72. Barsan, N.; Simion, C.; Heine, T.; Pokhrel, S.; Weimar, U. Modeling of sensing and transduction for p-type semiconducting metal oxide based gas sensors. *J. Electroceram.* **2010**, *25*, 11–19. [CrossRef]
73. Kim, H.J.; Lee, J.H. Highly sensitive and selective gas sensors using p-type oxide semiconductors: Overview. *Sens. Actuators B Chem.* **2014**, *192*, 607–627. [CrossRef]
74. Rana, M.K.; Sinha, M.; Panda, S. Gas sensing behavior of metal-phthalocyanines: Effects of electronic structure on sensitivity. *Chem. Phys.* **2018**, *513*, 23–34. [CrossRef]
75. Xiong, H.; Liu, B.; Zhang, H.; Qin, J. Theoretical insight into two-dimensional M-Pc monolayer as an excellent material for formaldehyde and phosgene sensing. *Appl. Surf. Sci.* **2021**, *543*, 148805. [CrossRef]
76. Kuprikova, N.M.; Klyamer, D.D.; Sukhikh, A.S.; Krasnov, P.O.; Mrsic, I.; Basova, T.V. Fluorosubstituted lead phthalocyanines: Crystal structure, spectral and sensing properties. *Dyes Pigments* **2020**, *173*, 107939. [CrossRef]

77. Chia, L.S.; Du, Y.H.; Palale, S.; Lee, P.S. Interaction of Copper Phthalocyanine with Nitrogen Dioxide and Ammonia Investigation Using X-ray Absorption Spectroscopy and Chemiresistive Gas Measurements. *ACS Omega* **2019**, *4*, 10388–10395. [CrossRef] [PubMed]
78. Koch, U.; Popelier, P.L.A. Characterization of C-H-O hydrogen bonds on the basis of the charge density. *J. Phys. Chem.* **1995**, *99*, 9747–9754. [CrossRef]
79. Kumar, P.S.V.; Raghavendra, V.; Subramanian, V. Bader's Theory of Atoms in Molecules (AIM) and its Applications to Chemical Bonding. *J. Chem. Sci.* **2016**, *128*, 1527–1536. [CrossRef]
80. Kaya, E.N.; Şenocak, A.; Klyamer, D.D.; Demirbaş, E.; Basova, T.V.; Durmuş, M. Ammonia sensing performance of thin films of cobalt(II) phthalocyanine bearing fluorinated substituents. *J. Mater. Sci. Mater. Electron.* **2019**, *8*, 7543–7551. [CrossRef]
81. Şenoğlu, S.; Özer, M.; Dumludağ, F.; Acar, N.; Salih, B.; Bekaroğlu, Ö. Synthesis, characterization, DFT study, conductivity and effects of humidity on CO2 sensing properties of the novel tetrakis-[2-(dibenzylamino)ethoxyl] substituted metallophthalocyanines. *Sens. Actuators B Chem.* **2020**, *310*, 127860. [CrossRef]
82. Liu, L.; Fei, T.; Guan, X.; Lin, X.; Zhao, H.; Zhang, T. Room temperature ammonia gas sensor based on ionic conductive biomass hydrogels. *Sens. Actuators B Chem.* **2020**, *320*, 128318. [CrossRef]
83. Can Ömür, B. Humidity effect on adsorption kinetics of ammonia onto electrospun SnO2 nanofibers. *Mater. Res. Express* **2019**, *6*, 045043. [CrossRef]
84. Sizun, T.; Bouvet, M.; Suisse, J.M. Humidity effect on ammonia sensing properties of substituted and unsubstituted cobalt phthalocyanines. *Talanta* **2012**, *97*, 318–324. [CrossRef] [PubMed]
85. Banimuslem, H.A.; Kadem, B.Y. Fluorinated chromium phthalocyanine thin films: Characterization and ammonia vapor detection. *Chemosensors* **2018**, *6*, 63. [CrossRef]
86. Basova, T.V.; Mikhaleva, N.S.; Hassan, A.K.; Kiselev, V.G. Thin films of fluorinated 3d-metal phthalocyanines as chemical sensors of ammonia: An optical spectroscopy study. *Sens. Actuators B Chem.* **2016**, *227*, 634–642. [CrossRef]